Abella, Mónica; Martínez, Cristóbal; Desco, Manuel; Vaquero, Juan José; Fessler, Jeffrey A. (2020). Simplified statistical image reconstruction for X-ray CT with beam-hardening artifact compensation. *IEEE Transactions on Medical Imaging*, 39(1), pp.: 111-118.

DOI: https://doi.org/10.1109/TMI.2019.2921929

Simplified Statistical Image Reconstruction for X-ray CT with Beam-Hardening Artifact Compensation

Monica Abella, Cristóbal Martínez, Manuel Desco, Juan José Vaquero, *Senior Member, IEEE,* and Jeffrey A. Fessler, *Senior Member, IEEE*

***Abstract*—CT images are often affected by beam-hardening artifacts due to the polychromatic nature of the X-ray spectra. These artifacts appear in the image as cupping in homogeneous areas and as dark bands between dense regions, such as bones. This paper proposes a simplified statistical reconstruction method for X-ray CT based on Poisson statistics that accounts for the non-linearities caused by beam hardening. The main advantages of the proposed method over previous algorithms is that it avoids the preliminary segmentation step, which can be tricky, especially for low-dose scans, and it does not require knowledge of the whole source spectrum, which is often unknown. Each voxel attenuation is modeled as a mixture of bone and soft tissue by defining density-dependent tissue fractions, maintaining one unknown per voxel. We approximate the energy-dependent attenuation corresponding to different combinations of bone and soft tissue, so called beam-hardening function, with the 1D function corresponding to water plus two parameters that can be tuned empirically. Results on both simulated data with Poisson sinogram noise and two rodent studies acquired with the ARGUS-CT system showed a beam hardening reduction (both cupping and dark bands) similar to analytical reconstruction followed by post-processing techniques, but with reduced noise and streaks in cases with low number of projections, as expected for statistical image reconstruction.**

***Index Terms*—X-ray computed tomography, polyenergetic, beam hardening, image reconstruction, penalized likelihood.**

Manuscript received September 2, 2018; revised October 23, 2018; accepted November 30, 2018. Date of publication May 20, 2019; date of current version June 6, 2019. This work was partially funded by NIH grants R01-HL-098686 and U01 EB018753, by Spanish Ministerio de Economia y Competitividad (projects TEC2013-47270-R and RTC-2014-3028-1) and the Spanish Ministerio de Economia, Industria y Competitividad (projects DPI2016-79075-R AEI/FEDER, UE - Agencia Estatal de Investigación and DTS17/00122 Instituto de Salud Carlos III - FIS), and co-financed by ERDF (FEDER) Funds from the European Commission, "A way of making Europe". The CNIC is supported by the Spanish Ministerio de Economia, Industria y Competitividad and the Pro CNIC Foundation, and is a Severo Ochoa Center of Excellence (SEV-2015-0505). (*Monica Abella and Cristóbal Martinez contributed equally to this work*). *(Corresponding author: Monica Abella).*

M. Abella, C. Martinez, J. J. Vaquero and M. Desco are with the Dpto. Bioingeniería e Ingeniería Aeroespacial, Universidad Carlos III de Madrid and the Instituto de Investigación Sanitaria Gregorio Marañón, Madrid, España (e-mail: mabella@ing.uc3m.es, crismart@pa.uc3m.es).

J. A. Fessler is with Electrical Engineering and Computer Science department, The University of Michigan, Ann Arbor, MI 48109-2122, USA (e-mail: fessler@umich.edu).

M. Abella and M. Desco are with the Centro Nacional de Investigaciones Cardiovasculares Carlos III (CNIC), Madrid, España (e-mail: monica.abella@cnic.es manuel.desco@cnic.es).

M. Desco is with the Centro de investigación en red salud mental (CIBERSAM), Madrid, España. (e-mail: desco@hggm.es).

I. Introduction

THE traditional image reconstruction method for X-ray CT, filtered back projection (FBP), faces challenges with non-standard scanning geometries like cone-beam and multi-slice helical CT and with truncated projection data. Statistical reconstruction methods are preferable for low-dose scans, can model any geometry and can accommodate measurement physics including beam hardening, partial-volume effects, and scatter [1], at the price of more computation time. X-ray tubes used in CT scanners are polyenergetic, producing a beam having a range of photon energies. Due to the energy dependence of mass attenuation coefficients, low-energy photons are preferably absorbed, causing a shift of the mean energy of the X-ray beam to higher values. Since attenuation coefficients are energy dependent, different projection measurements will 'see' the same object as having different attenuation values, leading to data inconsistencies in the Radon sense and, if uncorrected, reconstruction artifacts: 'cupping' in homogeneous areas, 'dark bands' or 'shadows' between bones, and 'spill over' of bone areas into soft tissue [2].

Most scanners use the 'linearization method', which assumes that all the materials in the scan field have X-ray attenuation characteristics equivalent to water, which are measured in a previous calibration [2]–[4]. This simplification leads to a suboptimal correction for inhomogeneous objects, especially in the presence of high-density areas, like bone. Dual-energy imaging enables quantitative CT reconstruction free of artifacts based on the acquisition of two scans at different voltages, typically 80 kVp and 120 kVp in clinical studies [5]–[7]. Although it is useful for tissue characterization, it needs longer scan times and/or more sophisticated scanner hardware, potentially increasing the dose significantly. Joseph and Spital [8] proposed a post-processing technique modeling the corrected data with a second-order polynomial dependent on the amount of bone traversed, which is obtained by a forward projection of the bone voxels segmented from an initial FBP reconstruction. This bone projection provides an estimate of the line-integral-dependent nonlinearity for each measurement that is then used to correct the projection data [8]–[11] followed by a second FBP. A similar approach was proposed in [12], but obtaining the linear combination in the image domain. Both approaches need knowledge of the spectrum and attenuation coefficients to find the optimum linear combination. Kyriakou et al. [13] obtained the optimum coefficients by maximizing the flatness

of the soft tissue, thus avoiding the need of spectral information. However, enforcing flatness in soft tissue areas may lead to a reduction of soft-tissue contrast. Following a similar idea, Park et al. [14] based the optimization of the coefficients on the minimization of the sparsity of the Laplacian. Schüller et al. [15] substituted the bone segmentation step required in the previous methods by an automatic histogram transformation to create the bone images. Optimum parameters are then obtained by minimizing the entropy of the image. Nevertheless, this method was shown to produce an overcompensation of the beam-hardening artifacts in real studies. In all the mentioned post-processing techniques, the result strongly depends on the quality of the bone segmentation, which may be challenging in low-dose studies or images highly affected by beam-hardening artifacts.

Alternatively, several iterative reconstruction methods inherently account for the nonlinearities of the beam-hardening effect. Yan et al. [16] developed an iterative non-statistical beam-hardening correction method, assuming two known substances and iteratively computing their volume fraction at each pixel. Elbakri and Fessler [17] presented a statistical algorithm also assuming that the sample was composed by known substances that had to be segmented in an initial image. They improved the method in [18] by including the segmentation in the cost function to be updated at each iteration and allowing pixels to contain mixtures. Both approaches needed tabulated measurements of the line integrals of bone and water over an appropriate range of object thicknesses for the CT system's spectrum. De Man et al. [1] proposed a statistical approach decomposing the linear attenuation coefficient into a photoelectric component and a Compton scatter component. The relative weight of these components was constrained based on prior material assumptions. The method did not require a preliminary bone segmentation but it still needed knowledge of the polyenergetic source spectrum. This was substituted by Srivastava and Fessler in [19] with the same calibration data and tuning parameters as Joseph and Spital. However, the proposed model makes an approximation that can lead to nonphysical negative values prone to cause convergence problems.

In an earlier conference paper [20], we explored in more depth the work in [19], proposed an improved approximation function, and presented preliminary 2D simulation results. The method modeled the tissue fractions in the voxels as functions of the density similarly to what was done in [18]. This paper improves the algorithm and illustrates its performance with real 3D CT data. The algorithm iteratively minimizes the Poisson likelihood, providing better solutions than PWLS [21], and uses ordered subsets [22] for acceleration. Including scatter estimates, if available, in the algorithm is straightforward. We tested the algorithm on simulated data under low-sampling conditions using synthetic phantoms and a CT of the anthropomorphic PBU-60 thorax phantom (Kyoto Kagaku Co., Kyoto, Japan). In addition, the algorithm was tested on two sparse-view rodent studies acquired with the CT subsystem of an ARGUS/CT (SEDECAL) scanner [23].

II. Materials and Method

We use the usual polyenergetic model [17] for the mean of the i-th measured sinogram data value

$$\overline{Y}_i = \int I_i(\varepsilon) e^{-\int_{L_i} \mu(x,y,z,\varepsilon)} d\varepsilon + r_i, \tag{1}$$

where μ(x,y,z,ε) denotes the unknown energy-dependent attenuation coefficient map of the object. The integral in the exponent is taken over the path of the i-th ray, L_i, and the "spectrum" $I_i(\varepsilon)$ incorporates the energy dependence of both the incident ray, a bowtie filter, and the detector sensitivity. The term ri can account for scatter and other background signals and is assumed known here. The goal is to reconstruct μ from the noisy measurements Y_i having mean given in (1).

A. Object model: Segmentation free implementation

For an object composed of K different substances, we express the attenuation coefficient at pixel j using the following model:

$$\mu_j(\varepsilon) = \sum_{k=1}^{K} m_k(\varepsilon) \rho_j f_k^j \tag{2}$$

where ρ_j denotes the unknown density, $m_k(\varepsilon)$ denotes the known mass attenuation coefficient of the k-th substance, and f_k^j denotes a unitless tissue fraction that quantifies the contribution of material k to attenuation in voxel j. As in previous methods, we assume that the object consists of only two substances: bone and soft tissue. The rationale behind this assumption comes from the dependence of the attenuation properties with energy for different tissues in the body, as most tissues behave like water and only bone differs significantly (see Fig. 1 in [18]).

To prevent an increase of the number of unknowns and avoid preliminary segmentation, we define a model for the tissue-fraction value in the pixel, f_k^j, as a function of the estimated density in that pixel, similarly to what was proposed in [18]. For the two-material case we assume

$$\begin{aligned} \mu_j(\varepsilon) \approx \sum_{k=1}^{2} m_k(\varepsilon) \rho_j f_k^j(\rho_j) = \\ \left(m_s(\varepsilon) f_s^j(\rho_j) + m_b(\varepsilon) f_b^j(\rho_j) \right) \rho_j, \end{aligned} \tag{3}$$

with tissue fraction functions, $f_s^j(\rho_j)$ and $f_b^j(\rho_j)$, built following the displacement model in [18] that considers materials occupying distinct spatial regions and mixed pixels at the boundaries. The soft-tissue fraction of the model in [18] was non zero for air, resulting in an increment of density values in air-filled areas inside the sample through subsequent iterations. To avoid it, we propose the piecewise third-order polynomials for the soft-tissue and bone fractions shown in Fig. 1, given by

$$f_S = \begin{cases} 0.336\rho + 16.234\rho^2 - 27.057\rho^3 & 0 \le \rho \le 0.4 \\ 1 & 0.4 \le \rho \le 1.1 \\ -54.29 + 133.6\rho - 105.5\rho^2 + 27.1\rho^3 & 1.1 \le \rho \le 1.5 \\ 0 & 1.5 \le \rho \end{cases} \tag{4}$$

$$f_B = \begin{cases} 0 & 0 \le \rho \le 1.1 \\ 55.3 + 133.6\rho + 105.5\rho^2 - 27.1\rho^3 & 1.1 \le \rho \le 1.5 \\ 1 & 1.5 \le \rho \end{cases} \quad (5)$$

where ρ has units g/cm^3. Taking into account the values provided by NIST, we assume soft tissue density is between 0.4 and 1.1 g/cm^3 and set a threshold for bone density of 1.5 g/cm^3. The coefficients were obtained as the result of a third-order polynomial fitting using a linear least-squares regression.

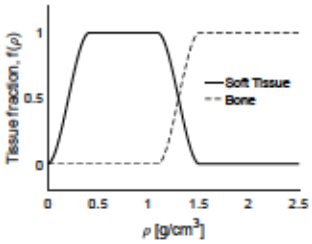

Fig. 1. Third-order polynomial tissue-fraction functions for soft tissue, $f_s(\rho)$, and bone, $f_b(\rho)$.

Based on (1) and (3), solving for the unknown values at each voxel requires knowledge of the X-ray spectrum emitted by the source, which is often difficult to characterize. The following section describes our proposal to overcome this problem.

B. Forward model: Beam hardening function

With the model explained above, we express (1), i.e., the mean of the measured data along the path of the i-th ray, L_i, as

$$\overline{Y}_i(\rho) = \int I_i(\varepsilon) e^{-m_s(\varepsilon) t_s^i(\rho) - m_b(\varepsilon) t_b^i(\rho)} d\varepsilon + r_i, \quad (6)$$

where $t_s^i(\rho)$ and $t_b^i(\rho)$ denote the contributions of each tissue type to the line integral along the i-th ray having units g/cm^2 and given by

$$t_s^i(\rho) = \sum_{j=1}^{p} a_{ij} f_s^j(\rho_j)\rho_j, \quad t_b^i(\rho) = \sum_{j=1}^{p} a_{ij} f_b^j(\rho_j)\rho_j, \quad (7)$$

where a_{ij} denotes elements of the system matrix (having units cm). Grouping the energy dependent terms into the exponent yields

$$\overline{Y}_i(\rho) = I_i e^{-F\left(t_s^i(\rho), t_b^i(\rho)\right)} + r_i; \quad I_i \equiv \int I_i(\varepsilon) d\varepsilon. \quad (8)$$

The function F characterizes the beam hardening and is defined by

$$F(t_s, t_b) = -\log\left(\int \frac{I(\varepsilon)}{I} \exp\left(-m_s(\varepsilon)t_s - m_b(\varepsilon)t_b\right) d\varepsilon\right), \quad (9)$$

where we drop the dependence on ray i for simplicity. One could calculate the *2D* function F analytically if the X-ray spectrum were known, which is often not the case. On the other hand, tabulating the 2D function experimentally would be cumbersome. Nevertheless, the 1D version of F corresponding to water, which has attenuation properties similar to soft tissue, is usually available for most scanners (Fig. 2).

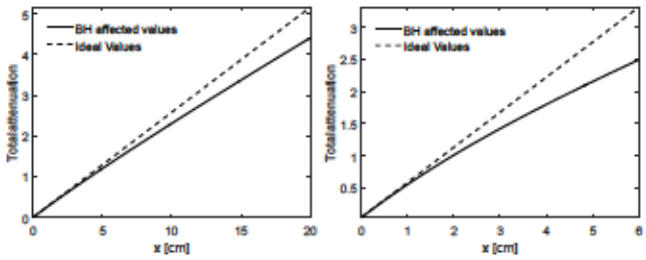

Fig. 2. Beam-hardening (BH) function used for the so-called water correction (linearization). Left: Simulation corresponding to water for a 100 kVp spectrum. Right: Calibration of the real scanner ARGUS/CT using a PMMA phantom for a 40 kVp spectrum.

We propose to approximate the complete 2D beam-hardening function by using the 1D function corresponding to water plus two additional parameters that we tune empirically. The idea is inspired by the post-reconstruction correction method of Joseph and Spital [8], which uses the concept of 'effective density', that is, the amount of water that would produce the same beam-hardening effect as the given amount of bone traversed. We introduce this concept in the forward model of an iterative algorithm by rewriting the beam hardening function as

$$F(t_s, t_b) = F(t_s + \sigma(t_s, t_b), 0) = F_w(t_e), \quad (10)$$

where $F_w(t)=F(t,0)$ is the beam hardening function corresponding to water and t_e is the line integral of the effective density, i.e. water equivalent.

The full X-ray spectrum would be needed to determine $\sigma(t_s,t_b)$ exactly, just like for the function $F(t_s,t_b)$. Fig. 3 shows calculated plots of $\sigma(t_s,t_b)$ for a typical polyenergetic spectrum.

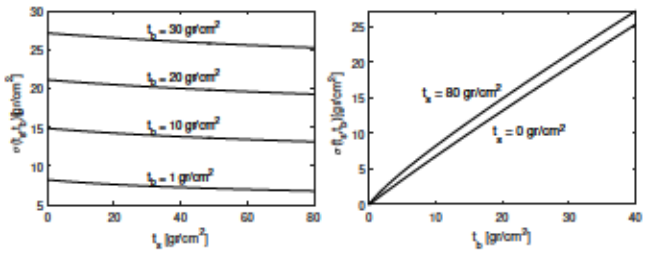

Fig. 3. Simulation of $\sigma(t_s,t_b)$. Left: profiles versus ts where each line corresponds to different values of t_b. Right: profiles versus t_b corresponding to the minimum and maximum t_s values.

As we can see in the left panel of Fig. 3, the dependence on t_s can be considered negligible when the amount of bone in the object is small, which is the case in clinical studies. Joseph and Spital suggested in [8] a power series approximation of the function that defines the measured projection depending only on t_b. Hsieh [10] described a similar approach, based on

$$\sigma_1(t_b) = At_b - Bt_b^2, \quad (11)$$

where A and B are parameters that one can tune. Although approximation (12) works adequately for FBP reconstruction, it can fail when used in the forward model of a statistical reconstruction method because it can yield negative values.

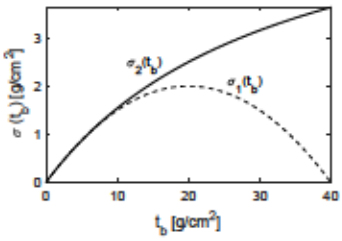

Fig. 4. Two examples of approximations for $\sigma(t_s, t_b)$.

Furthermore, one can verify that $\sigma(t_s,t_b)$ is a monotone increasing function of both of its arguments, whereas (11) is not (see Fig. 4). To overcome this drawback of (11), we investigated the following alternative approximation:

$$\sigma_2(t_b) = \frac{A t_b}{1 + \frac{B}{A} t_b}, \tag{12}$$

where, as in (11), A is unitless and B has units cm^2/g. This function is monotone nonnegative and matches (10) for small values of t_b. Substituting (12) into (10) and (8) leads to our proposed forward model:

$$\overline{Y}_i(\rho) = I_i e^{-F_w\left(t_s^i(\rho) + \frac{A t_b^i(\rho)}{1+\frac{B}{A} t_b^i(\rho)}\right)} + r_i = I_i e^{-F_w\left(\sum_{j=1}^{P} a_{ij} f_s^j(\rho_j)\rho_j + \frac{A \sum_{j=1}^{P} a_{ij} f_b^j(\rho_j)\rho_j}{1+\frac{B}{A}\sum_{j=1}^{P} a_{ij} f_b^j(\rho_j)\rho_j}\right)} + r_i. \tag{13}$$

C. Algorithm

An accurate model of the physics of CT acquisition needs to account for the energy-integrating detection process and the additive detector read-out noise. On the other hand, sophisticated models often lead to more difficulties in optimizing the associated penalized-likelihood. For simplicity, in this work we approximate the measurement statistics as independently distributed Poisson random variables [24]:

$$Y_i \sim Poisson\left\{\overline{Y}_i\right\}, \quad i = 1, ..., N \tag{14}$$

The corresponding negative log-likelihood for independent Poisson measurements is given by

$$-L(\rho) = \sum_{i=1}^{N} h_i\left(F_w(t_e(\rho))\right) \tag{15}$$

with

$$h_i(l) = -Y_i \log\left(I_i e^{-l} + r_i\right) + I_i e^{-l} + r_i, \tag{16}$$

where r accounts for mean contamination by extra background counts caused primarily by scatter. Because data is noisy and tomography is an ill-posed problem, we use regularization by adding a penalty term to the likelihood function that controls how much the object ρ departs from prior assumptions about image properties. In this work we used a 3D roughness penalty function with the convex edge-preserving Huber potential:

$$R(\rho) = \sum_{j=1}^{N_p} \frac{1}{2} \sum_{k \in N_j} w_{jk} \cdot \psi(\rho_j - \rho_k); \qquad \psi(t) = \begin{cases} \frac{|t|^2}{\delta} & |t| \le \delta \\ \delta|t| - \frac{\delta}{2} & |t| > \delta \end{cases}, \tag{17}$$

where N_j is a neighborhood of pixels near pixel j, w_{jk}=w_{kj} and ψ is the convex edge-preserving Huber potential. This penalty function is modified as described in [25] to improve spatial resolution uniformity. The penalized cost function is now:

$$\Phi(\rho) = -L(\rho) + \beta R(\rho), \tag{18}$$

where the scalar parameter β controls the tradeoff between the data-fit and penalty terms.

We derived an iterative algorithm based on separable quadratic surrogates using the principles of optimization transfer [26], resulting in the following update:

$$\rho^{n+1} = \rho^n - D^{-1} \nabla \Phi(\rho^n), \tag{19}$$

where D is a diagonal matrix that influences the rate of convergence. Instead of designing D to ensure that the algorithm monotonically decreases the cost function we choose the elements of D approximately as suggested in [17][26] by using the following pre-computed curvature:

$$d_j = \left(K m_s(\varepsilon_{eff})\right)^2 \sum_{i=1}^{N} a_{ij} \left(\sum_j a_{ij}\right) Y_i, \tag{20}$$

where we include K as tuning parameter for the step size.

The final algorithm is shown in Algorithm 1, where *DReg* and *D2Reg* are first and second order derivatives of the surrogate of the regularization term as explained in [24] and G is the system matrix. Four projections and one backprojection are performed at each iteration.

Algorithm 1 Proposed algorithm

```
x=fbpu
denom=G'*(yi.*(G*(ones(size(x)))))
for 1 to iterations
hxs = x*fs(x)
hxt = x*ft(x)
hxsDeriv = x*Dfs(x)
hxtDeriv = x*Dft(x)
ti = G*hxt
si = G*hxs
te = si+sigma(A,B,ti)
F = fw(te)
hFs = Dfw(te)
m = I*exp(-F)+r
Ni = (y/m-1)*I*exp(-F)
Njs = hFs*Ni;
NjAux1 = G*(fs(x)+hxDeriv)
NjAux2 = G*(ft(x)+hxtDeriv)
NjAux = NjAux1+Dsigma(A,B,ti)*NjAux2
Nj = G'*(NjAux*Njs)
num = Nj+beta*DReg
den = denoms*(K*Dfw(0))^2+ beta*D2Reg
x = x+num/den
x = max(x,0)
end
```

We use an ordered subsets approximation of (19) to increase speed [22]. The 2D version on this algorithm will be incorporated to the Michigan Image Reconstruction Toolbox (MIRT), available at http://www.eecs.umich.edu/~fessler/code.

D. Performance assessment

We simulated four polyenergetic spectra, with 80, 100, 120 and 140 kVp, and 0.25 cm aluminum filtration at the source to give a spectrum shape similar to clinical practice (Fig. 5).

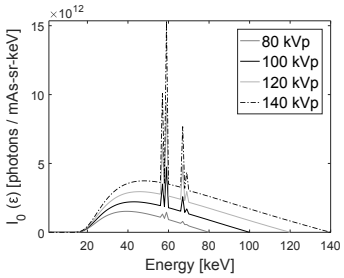

Fig. 5. X-ray spectra used for simulations.

Based on this model for the source, we generated a set of transmission polyenergetic Poisson X-ray projections with parallel beam geometry using the MIRT toolbox.

The detector was modeled as a simple photon-counting device. The projection data had 512 radial bins with 0.1 cm ray spacing and 180 angular steps over 180 degrees. We did not simulate scatter. The blank scan value was 10^6 and 10^5 counts per detector element to simulate high- and low-SNR scenarios respectively.

We first evaluated if our approach in (12) is physically reasonable using a basic ellipsoidal phantom made of water, with density 1.0 g/cm^3, containing two disks of bone, with density 1.9 g/cm^3. We tested A values from 0 to 2 in steps of 0.001 and B from 0 to 0.1 cm^2/g in steps of 0.001 cm^2/g. The optimum A and B were those that minimized the root mean square error (RMSE) with respect to the FBP reconstruction from monoenergetic data (reference image) measured in the rectangle shown in the left panel of Fig. 6. We then evaluated the dependency of these values with bone size using them to reconstruct a phantom made of soft tissue with bone inserts of different sizes and densities equal to 1.9 g/cm3 and 2.1 g/cm^3 and two inserts of fat with density 0.95 g/cm^3, shown in middle panel of Fig. 6. We used the same phantom to evaluate the performance of the method under low-SNR and low-sampling conditions, using 45 projections over 180 degrees.

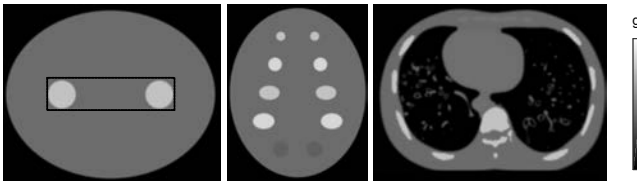

Fig. 6. Left: Ellipsoidal phantom made of soft tissue with 30 cm and 20 cm diameter sizes and two bone inserts with 4 cm diameter; dotted lines indicate areas used for measurements. Middle: Phantom with inserts of different sizes and densities. Right: Slice of the PBU-60 thorax phantom.

We used the same A and B values on simulated human data using a slice of the PBU-60 thorax phantom (right panel of Fig. 6). Density values for bone areas (spine and ribs) and soft tissue were 1.9 g/cm^3 and 1.06 g/cm^3 respectively.

We reconstructed the data using uncorrected FBP, water-corrected FBP, FBP corrected by the Joseph and Spital (JS) method, a monoenergetic statistical algorithm (ordered subsets separable paraboloidal surrogates [26]), and the proposed polyenergetic algorithm. We used a Hanning window with cut-off frequency of 80% Nyquist in the FBP reconstruction to achieve a spatial resolution comparable to that of the statistical algorithms. Tissue fraction functions shown in Fig. 1 were applied to the water-corrected FBP image providing the segmentation required by the JS technique. The proposed method ran for 50 iterations, β = 30 and δ = 0.002 g/cm^3 for high-SNR and 100 iterations, β = 145 and δ = 0.002 g/cm^3 for low-SNR and low-sampling in (17) and (18). The monoenergetic method ran for 50 iterations with 15 subsets, β = 4 and δ = 0.001 g/cm^3. We chose constants A = 1.475 and B = 0.0100 cm^2/g in (14).

In addition to qualitative assessment of artifact reduction, we quantified the performance in terms of noise, streaks due to undersampling and bias of the different algorithms. Noise and undersampling-induced streaks were assessed as the coefficient of variation (CV) in the homogeneous region depicted in the left panel of Fig. 7. Bias was calculated as the RMSE relative to the reference image for the whole soft-tissue area (middle panel of Fig. 7) and for the area with the strongest beam hardening artifact, close to the ribs (right panel of Fig. 7).

Fig. 7. ROIs obtained by thresholding and erosion/dilation to measure CV (A), and RMSE (B and C) in soft tissue.

Finally, the algorithm was tested on two rodent studies acquired with the CT subsystem of an ARGUS/CT (SEDECAL) scanner, a cone-beam micro-CT scanner based on a flat-panel detector [23]. We focus on low-SNR and sparse-sampling scenarios because these are the cases that derive the greatest benefit from iterative methods such as that proposed.

We obtained 180 views of a volume of 516×516×301 voxels with 0.121 mm^3 voxel size, covering 360 degrees with a source voltage of 40 keV. We reconstructed the images using uncorrected FDK, JS-corrected FDK, the monoenergetic statistical algorithm and the proposed polyenergetic algorithm. A 3D version of these algorithms was implemented substituting the MIRT-CPU kernels by the GPU-accelerated kernels from FUX-Sim [27]. We obtained the segmentation required by the JS technique using the same tissue fractions used for the proposed method, shown in Fig. 1, on the water corrected FDK image.

Parameters in this case were A = 2.458 and B = 0.49 cm^2/g in (14) and β = 0.06 and δ = 0.04 g/cm^3 for the proposed method and β = 0.55 and δ = 0.02 g/cm^3 for the monoenergetic algorithm in (17) and (18).

Both monoenergetic and proposed polyenergetic methods were ran for 200 iterations on a computer with an Intel Core i7-4790 CPU, 32 GB RAM and an NVIDIA GeForce GTX960. Runtime was 70 and 100 seconds per iteration, respectively. The reason for higher computational burden of the polyenergetic algorithm, compared to the monoenergetic

TABLE I
OPTIMIZED A AND B PARAMETERS FOR DIFFERENT VOLTAGES

Voltage	JS method		Proposed method	
(kVp)	A	B (cm^2/g)	A	B (cm^2/g)
140	0.228	0.0045	1.3	0.0075
120	0.275	0.0045	1.4	0.01
100	0.335	0.0045	1.475	0.01
80	0.41	0.0045	1.8	0.0325

case, is the higher number of projections per iteration needed. No effort was made to optimize execution time.

III. Results

Table 1 shows the optimum A and B values found for each voltage with simulations using the ellipsoidal phantom. Fig. 8 shows good beam-hardening artifact compensation achieved by the proposed algorithm for different sizes and densities of bone, proving the feasibility of the approximation of the σ function. For the low-SNR and low-sampling case, we can also see a dramatic reduction of the undersampling-induced streaks.

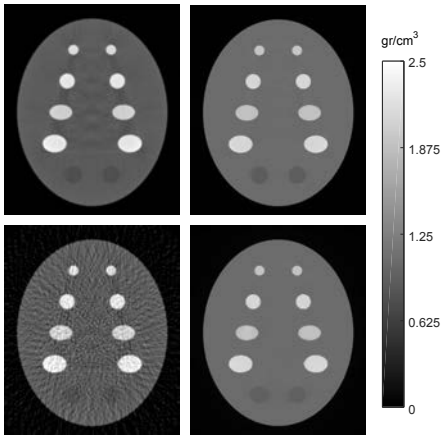

Fig. 8. Phantom with different bone sizes reconstructed with FBP (left) and with the proposed algorithm (right) for the high-SNR (top) and low-SNR and low-sampling (bottom) cases.

Fig. 9 shows the absolute differences between the reference and the results of the FBP and the proposed algorithm.

Fig. 10 shows the evolution of the soft-tissue and bone masks along iterations for the low-dose and low-sampling case. We can see the improvement of the soft tissue and bone segmentations through iterations, where both dark bands and undersampling streaks are reduced, resulting in a more accurate model.

Figs. 11 and 12 show the results on one slice of the PBU-60 thorax phantom. The uncorrected FBP image suffered from beam-hardening artifacts in the form of dark bands between the ribs and spine. The statistical iterative reconstruction with no modeling of the polyenergetic spectrum exhibited significantly lower CV (noise and undersampling-based streaks) but still suffered from beam-hardening artifacts. The proposed method eliminates the beam-hardening artifacts, removing the dark bands and recovering the real soft tissue values, while showing a significant reduction of noise and streaks when compared with the post-processing JS method.

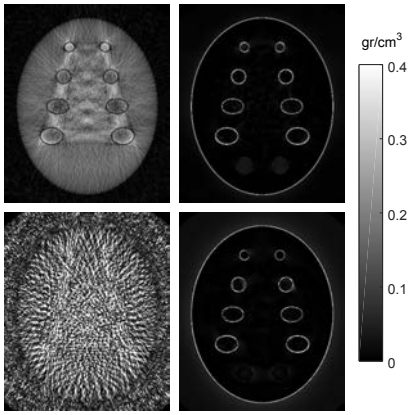

Fig. 9. Absolute difference between the reference and the result of the proposed algorithm (top) and the FBP (bottom) for the low-SNR and low-sampling (left) and the high-SNR (right) cases.

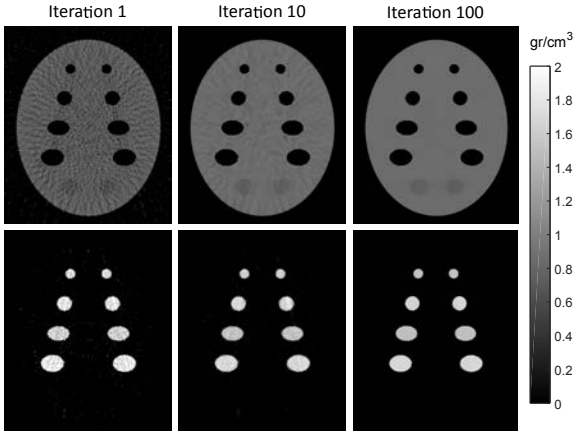

Fig. 10. Soft-tissue and bone segmentations for the low-dose and low-sampling case at different iterations.

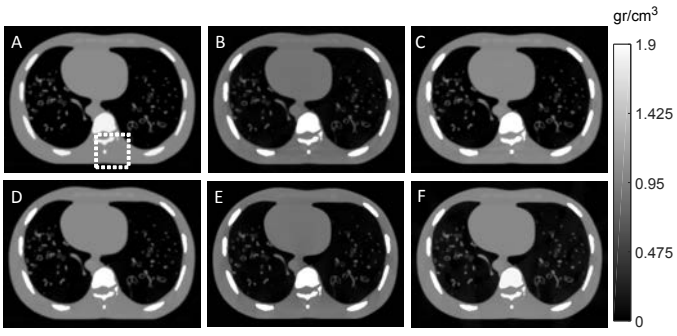

Fig. 11. 512x512 pixel axial slice of the PBU-60 phantom (A), reconstructed with FBP (B), FBP+Water correction (C), FBP+JS correction (D), statistical algorithm using a model incorrectly based on a monoenergetic X-ray source (E) and the proposed algorithm (F).

Table 2 shows the results of the analysis of noise, streaks and bias for all the methods. The proposed method achieved a bias reduction on the same order as the JS method, but with a significantly higher CV reduction in the soft-tissue area. There

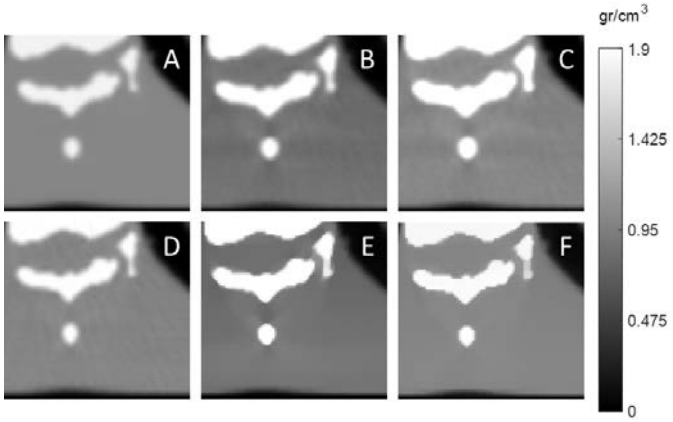

Fig. 12. Zoom-in view of the area inside the dotted square drawn in Fig. 8 A for images A-F.

TABLE II
CV AND RMSE RESULTS FOR THE PBU-60 PHANTOM

Method	CV[a,b] in soft tissue (ROI A)	RMSE[b] in soft tissue (ROI B)	RMSE[b] close to ribs (ROI C)
FBP	0.032	0.164	0.178
FBP + water	0.041	0.104	0.175
FBP + JS	0.040	0.046	0.055
Monoenergetic	0.030	0.159	0.179
Proposed method	0.029	0.038	0.052

[a]Coefficient of variation. [b]Units of density g/cm^3.

was also a significant reduction of CV in the background, not visible in Fig. 11 because the window was selected to show beam-hardening artifacts. The monoenergetic iterative algorithm resulted in a similar CV reduction as the proposed method, as expected, but with no bias reduction mainly due to the beam-hardening effects.

Fig. 13 shows the results for the two rodent studies. Again, the statistical iterative reconstruction with no modeling of the polyenergetic spectrum exhibits significantly better noise and streaks behavior than the FDK-based methods but still suffers from beam-hardening artifact. The proposed method eliminates the beam-hardening artifact while showing a significant reduction of noise and streaks when compared with the post-processing JS method.

IV. Discussion

This work presents a new statistical reconstruction algorithm for X-ray CT that accounts for beam-hardening effect.

In most of the previously proposed methods the forward model requires knowledge of the X-ray source spectrum, which is often unknown in practice. To overcome this problem, we modify the projection model by adapting one idea previously proposed by Joseph and Spital [8]. This idea is based on the concept of "effective water path length". We substitute the 2D beam-hardening function corresponding to bone and soft tissue with the 1D function corresponding to water, already available in most scanners, plus two empirical parameters, A and B in (13). This theoretical model is thus exact for monochromatic radiation and represents an approximation in the polychromatic case. The approximation of $\sigma(t_s, t_b)$ used here ignores the dependence on t_s, which is a rather accurate assumption when there are only small areas of bone. Future works might explore more accurate approximations by including the dependence with t_s in the model. In our implementation, the parameters A and B were obtained empirically, but it could be interesting to investigate the possible inclusion of these parameters in the algorithm in order to perform a joint estimation.

Regarding the model of the object, the most commonly used approach is to assume that each voxel can only be either bone or soft tissue and to segment bone from a preliminary reconstruction obtained with a fast algorithm such as filtered back-projection. This segmentation can be challenging, especially in the case of low-dose scans, which suffer from low SNR and possibly photon starvation. Furthermore, this model neglects partial volume effects, as voxels are not allowed to contain a mixture of bone and soft tissue. Our approach addresses these problems, as we model the attenuation at each voxel by defining piecewise density-dependent tissue fractions, which are updated at each iteration, eliminating possible segmentation problems in low-dose studies. In our work, selection of the intervals for these functions was based on the typical densities for soft-tissue and cortical bone found in NIST. Further evaluation of the effect of the definition of these intervals on the recovered density values for both clinical and preclinical data is warranted. Although the bone/soft-tissue model will suffice for most cases, a three-class model could be necessary when contrast agents or metallic implants are present. It might also help to improve the estimation of the density of fat.

Comparing panels B, C, and D of Fig. 13, it is clear that the reduction in undersampling-induced streaks and noise using the statistical method is likely due to noise model and the edge-preserving penalty, and not a novel result in itself. The main point are the reduced beam-hardening artifacts going from Fig. 13-C to Fig. 13-D. We used a noise model based on simple Poisson statistics for simplicity, but it does not reflect the actual physics of CT acquisition. The strategy proposed in (13) also can be used with more accurate statistical models that account for energy-integrating detection and additive detector read-out noise, which could improve the accuracy of reconstruction. One possibility would be a model that considers the total signal to be a sum of energy-scaled Poisson processes, each with a different scale factor. This model is potentially more accurate because it accounts for the polyenergetic nature of the incident beam in the detection process. Nevertheless, sophisticated models often lead to more difficulties in optimizing the associated penalized-likelihood. Although scattering was not considered in this work, including scatter estimates in the algorithm is straightforward.

V. Conclusion

We present a new statistical reconstruction algorithm for polyenergetic X-ray CT based on Poisson statistics and a physical model that accounts for the nonlinearities caused

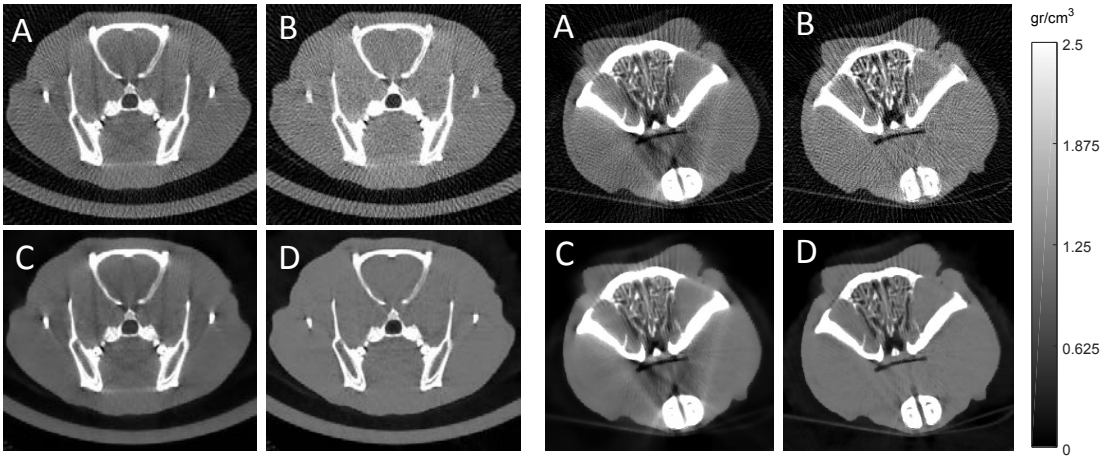

Fig. 13. Axial slice of two rodent studies reconstructed with uncorrected FDK (A), FDK+JS (B), the monoenergetic iterative algorithm (C), and the proposed method (D).

by the beam-hardening effect. The main advantage of our method over previously proposed iterative algorithms is the combination of two desirable characteristics: 1) it eliminates the problem of wrong bone segmentations in low-dose studies or images highly affected by beam-hardening artifacts, and 2) it corrects beam-hardening artifacts without requiring knowledge of the X-ray source spectrum. Results showed a similar beam-hardening correction as the post-processing technique proposed by Joseph and Spital, but with reduced noise and streak artifacts in the low-dose, low-sampling cases, as expected for statistical image reconstruction with Huber penalty with edge-preserving regularization.

REFERENCES

[1] B. De Man, J. Nuyts, P. Dupont, G. Marchal, and P. Suetens, "An iterative maximum-likelihood polychromatic algorithm for ct," *IEEE Trans. Med. Imaging*, vol. 20, no. 10, pp. 999–1008, 2001.

[2] R. A. Brooks and G. Di Chiro, "Beam hardening in x-ray reconstruction tomography," *Phys. Med. Biol.*, vol. 21, pp. 390–8, 1976.

[3] G. T. Herman, "Correction for beam hardening in computed tomography," *Phys. Med. Biol.*, vol. 24, no. 1, pp. 81–106, 1979.

[4] W. D. McDavid, R. G. Waggener, W. H. Payne, and M. J. Denis, "Correction for spectral artifacts in cross-sectional reconstruction from x-rays," *Med. Phys.*, vol. 4, no. 1, p. 54–7, 1997.

[5] R. E. Alvarez and A. Macovski, "Energy-selective reconstruction in x-ray computerized tomography," *Phys. Med. Biol.*, vol. 21, no. 5, p. 733–44, 1976.

[6] J. A. Fessler, I. A. Elbakri, P. Sukovic, and N. H. Clinthorne, "Maximum-likelihood dual-energy tomographic image reconstruction," *Proc. SPIE*, vol. 4684, no. 1, pp. 38–49, 2002.

[7] P. Sukovic and N. H. Clinthorne, "Design of an experimental system for dual energy x-ray ct," in *1999 IEEE Nuclear Science Symposium. Conference Record. 1999 Nuclear Science Symposium and Medical Imaging Conference (Cat. No. 99CH37019)*, vol. 2. IEEE, 1999, pp. 1021–1022.

[8] P. M. Joseph and R. D. Spital, "A method for correcting bone induced artifacts in computed tomography scanners," *J. Comp. Assisted Tomo.*, vol. 2, no. 1, pp. 100–8, 1978.

[9] P. M. Joseph and C. Ruth, "A method for simultaneous correction of spectrum hardening artifacts in ct images containing both bone and iodine," *Med. Phys.*, vol. 24, no. 10, pp. 1629–34, 1997.

[10] J. Hsieh, R. C. Molthen, C. A. Dawson, and R. H. Johnson, "An iterative approach to the beam hardening correction in cone beam ct," *Med. Phys.*, vol. 27, no. 1, pp. 23–29, 2000.

[11] O. Nalcioglu and R. Y. Lou, "Post-reconstruction method for beam hardening in computerised tomography," *Phys. Med. Biol.*, vol. 24, no. 2, pp. 330–40, 1979.

[12] G. T. Herman and S. S. Trivedi, "A comparative study of two postreconstruction beam hardening correction methods," *IEEE transactions on medical imaging*, vol. 2, no. 3, pp. 128–135, 1983.

[13] Y. Kyriakou, E. Meyer, D. Prell, and M. Kachelrieß, "Empirical beam hardening correction (ebhc) for ct," *Medical physics*, vol. 37, no. 10, pp. 5179–5187, 2010.

[14] H. S. Park, D. Hwang, and J. K. Seo, "Metal artifact reduction for polychromatic x-ray ct based on a beam-hardening corrector," *IEEE transactions on medical imaging*, vol. 35, no. 2, pp. 480–487, 2016.

[15] S. Schuller, S. Sawall, K. Stannigel, M. Hulsbusch, J. Ulrici, E. Hell, and M. Kachelriess, "Segmentation-free empirical beam hardening correction for ct," *Med Phys*, vol. 42, no. 2, pp. 794–803, 2015. [Online]. Available: http://www.ncbi.nlm.nih.gov/pubmed/25652493

[16] C. H. Yan, R. T. Whalen, G. S. Beaupré, S. Y. Yen, and S. Napel, "Reconstruction algorithm for polychromatic ct imaging: application to beam hardening correction," *IEEE Trans. Med. Imaging*, vol. 19, p. 1–11, 2000.

[17] I. A. Elbakri and J. A. Fessler, "Statistical image reconstruction for polyenergetic x-ray computed tomography," *IEEE Trans. Med. Imaging*, vol. 21, no. 2, pp. 89–99, 2002.

[18] ——, "Segmentation-free statistical image reconstruction for polyenergetic x-ray computed tomography with experimental validation," *Physics in Medicine & Biology*, vol. 48, no. 15, p. 2453, 2003.

[19] S. Srivastava and J. A. Fessler, "Simplied statistical image reconstruction algorithm for polyenergetic x-ray ct," pp. 1551–5, 2005.

[20] M. Abella and J. A. Fessler, "A new statistical image reconstruction algorithm for polyenergetic x-ray ct," *Proceedings of the 2009 IEEE International Symposium on Biomedical Imaging (ISBI)*, pp. 165–8, 2009.

[21] P. J. La Rivière, J. Bian, and P. A. Vargas, "Penalized-likelihood sinogram restoration for computed tomography," *IEEE transactions on medical imaging*, vol. 25, no. 8, pp. 1022–1036, 2006.

[22] H. M. Hudson and R. S. Larkin, "Accelerated image reconstruction using ordered subsets of projection data," *IEEE Trans. Med. Imaging*, vol. 13, no. 4, pp. 601–9, 1994.

[23] J. J. Vaquero, S. Redondo, E. Lage, M. Abella, A. Sisniega, G. Tapias, M. L. S. Montenegro, and M. Desco, "Assessment of a new high-performance small- animal x-ray tomograph," *IEEE Trans Nucl Sci*, vol. 55, no. 3, pp. 898–905, 2008.

[24] H. Erdogan and J. A. Fessler, "Monotonic algorithms for transmission tomography," *IEEE Trans. Med. Imaging*, vol. 18, no. 9, pp. 801–14, 1999.

[25] J. A. Fessler, "Mean and variance of implicitly defined biased estimators (such as penalized maximum likelihood): Applications to tomography," *IEEE Trans. Image Proc.*, vol. 5, no. 3, p. 493–506, 1996.

[26] H. Erdogan and J. A. Fessler, "Ordered subsets algorithms for transmission tomography," *Phys. Med. Biol.*, vol. 44, pp. 2835–51, 1999.

[27] M. Abella, E. Serrano, J. Garcia-Blas, I. García, C. de Molina, J. Carretero, and M. Desco, "Fux-sim: An implementation of a fast universal simulation/reconstruction framework for x-ray systems," *Plos One*, vol. 12, no. 7, p. e0180363, 2017.